university of groningen / faculty of science and engineering

Master Studies in Theoretical Chemistry and Computational Modelling

Multiscale modeling of optical spectra in the chlorosomal light-harvesting system

Master Thesis

For the Theoretical Chemistry and Computational Modeling Programme
Cohort 2020-2022

by

Jorge Luis Castro Angamarca

S4480805

Supervisor/First Examiner:

prof. dr. T.L.C.Jansen

Second Examiner:

prof. dr. R.W.A. Havenith

Abstract

Linear Absorption, Linear Dichroism, and two-dimensional electronic spectra at different polarization combinations were simulated to determine spectral signatures of superradiant degenerate states associated with the cylindrical symmetry and chirality of triple-walled tubular aggregates of bacteriochlorophyll *c*, emulating the light-harvesting complex of *Chlorobaculum Tepidum* bacterial chlorosome. A combination of molecular dynamics simulations and excitonic Frenkel Hamiltonians through a multiscale approach based on the point-dipole approximation was employed to study realistic-sized tube structures with pre-defined chiralities. Spectral features, which intensities depend on the system's chirality and overall structure, were found in this research. Results strongly suggest that the chirality of the chlorosome's light-harvesting system and other structural features related to the orientation of transition dipoles in molecular aggregates can be further studied experimentally and computationally using cross-polarized two-dimensional electronic spectroscopy techniques.

Contents

Chapter 1

Introduction

In order to efficiently collect incoming sunlight, photosynthetic organisms have developed various types of light-harvesting (LH) antennas where pigments are often held in appropriate positions by sophisticated protein complexes [1]. A striking exception to this architecture is represented by the chlorosomal light-harvesting system adopted by some species of green sulfur bacteria [2,3]. The number of chromophores in other light-harvesting antennas usually does not exceed a few hundred. In contrast, the interior of a single chlorosome is composed of a much larger number ($\sim 10^5$) of strongly coupled bacteriochlorophyll (BChl) molecules (c, d, or e, depending on the methylation of the chromophore) that self-assemble into pseudosymmetric syn-anti parallel stacks forming predominantly concentric tubular tubes [4,5], as seen in Figure 1.1.

Structurally, the chlorosome's LH antennae can be seen as an aggregate of N-molecules occupying a 2D lattice rolled onto a cylinder surface. The lattice is defined by the basis vectors $\vec{a}$ and $\vec{b}$ and the angle γ between them [6]. The cylindrical structure is formed by rolling the lattice in a certain direction given by the so-called *Chiral* vector $\vec{C}$ defined in terms of the lattice vectors, as shown in Figure 2.1. The radius R of the cylinder is obtained from the norm of the chiral vector as $|C| = 2\pi R$. Due to the dense packing of chromophores in the cylinder, the excited states responsible for light absorption are strongly coupled. It leads to the delocalization of excitation quanta over several molecules [7]. These collective excited states, known as molecular excitons, are at the heart of the efficient transfer of the energy absorbed by the antenna and determine the optical properties of the chlorosomes, as revealed by pump-probe [8] and two-dimensional electronic spectroscopy (2DES) [9]. The packing of chromophores in cylindrical aggregates is macroscopically characterized by their chirality, i.e., the angle δ between the reference axis of the 2D lattice

and the rolling (chiral) vector, and is experimentally measured using cryogenic electronic microscopy (cryo-EM) [2]. On the other hand, the relative orientation of the chromophores in a microscopic picture is better characterized by the angle β between the monomer transition-dipole moments (TDMs) and the symmetry axis of the cylinder determined by optical spectroscopy techniques [10].

Further understanding of these systems can potentially be exploited for more efficient, sustainable, and environmentally clean ways of converting solar energy via the rational design of molecular components for artificial photosynthesis. Subsequently, strong efforts have been devoted to elucidating the interplay of structural and dynamical properties that enables an amazing quantum efficiency for transfer within and between tubes. However, the large degree of structural heterogeneity and the lack of a distinct crystalline organization hampers experimental characterization preventing the elucidation of a direct structure-property relation.

Although the parallel syn-anti stack of pigments in a 2D lattice has been demonstrated by solid-state NMR [4], the arrangement of secondary structures is still poorly understood [11, 12]. Cryo-EM experiments in the chlorosomes from the wild type (WT) and a triple mutant (bchQRU) of the green sulfur bacteria *Chlorobaculum Tepidum* have reported superstructures with chiralities of $\delta = 90°$ and $\delta = 0°$ respectively [2]. Moreover, the same study established that the helical nature of the chlorosome is conserved upon variation of the BChl composition. A combination of polarization-resolved, single-particle fluorescence-excitation spectroscopy and theoretical modeling for a more homogeneous bchR mutant yielded a packing of the BChl *c* molecules in tubular symmetry such that the angle β is about 55° [10]. It was in close agreement with the proposed structure of the bchQRU triple mutant. However, the computational combination of the optical spectroscopy data with results previously obtained from NMR spectroscopy and cryo-electron microscopy led to a macroscopic chirality of $\delta \approx 70°$ (or $\delta \approx 110°$ in the framework employed in this project) for the bchR mutant, in disagreement with results expected from NMR and cryo-EM solely.

The mismatch between the macro and microscopic results suggests that an unambiguous description of the molecular packing of BChl within chlorosomes requires the combination of information obtained at different levels of description. In this context, a computational multiscale approach combining quantum mechanical and classical descriptions represents an important tool for the assignment of the packing order of the BChl assembly. Indeed, the computational calculation of spectra based on the Frenkel excitonic Hamiltonian has already played a major role in studying photoinduced processes in other composite systems

[1, 13].

As will be shown in Chapter 2, an extension of the Frenkel exciton theory to cylindrical molecular aggregates predicts the existence of three superradiant states [7] that contribute to their optical and electronic spectra. These are associated with two degenerate exciton states with wave numbers $k = \pm 1$ and a non-degenerate exciton state of wave number $k = 0$. The dipoles of these states are oriented perpendicular and parallel to the cylinder's major axis, respectively. The signals originating from $k = \pm 1$ states give equal contributions to optical spectra and are less intense than the state $k = 0$ due to their degeneracy. Consequently, they are lost in the ensemble-averaged spectra [7].

Nevertheless, they are expected to contribute to optical spectral signals since they are dipole-allowed. The contribution amount depends on the magnitude of the associated TDMs oriented parallel and perpendicular to the cylinder's main axis. The ratio of the oscillator strengths along the two principal directions is directly related to the angle β [7] and, as will be shown in this work, to the system's chirality. In this context, the *in silico* experiments and simulations in Chapter 4 aim to clarify the spectral fingerprints of the chlorosome's LH complex while providing means to study the effects of chirality on the functional properties of the tubular molecular aggregates, experimentally and computationally. The interplay between the eigenstates and the chirality of chlorosomal tube aggregates found in this work gave rise to a spectral observable that could be used for discriminating between cylindrical structures with different chiralities, in complement of the previously mentioned techniques.

1.1 Outline

This project used time trajectories obtained from molecular dynamics (MD) simulations to build the multiscale excitonic Hamiltonians of a set of pre-assembled BChl *c* cylindric aggregates. The Hamiltonians were used as input for the Numerical Integration of Schrödinger Equation (NISE) algorithm [14–16] to calculate the spectra of linear absorption and linear dichroism (LD), as well as two-dimensional electronic spectroscopy (2DES)in parallel, perpendicular, and cross-polarization schemes. Further treatment of calculated spectra was carried out to interpret the experimental data and ultimately determine spectral signatures of the interplay among the $k \pm 1$ degenerate states and the system's chirality in the electronic spectra of the chlorosome's LH complex.

In Chapter 2, a deeper analysis of the geometrical formulation of the Frenkel Hamil-

tonian for a cylindrical arrangement of chromophores is provided. The quantum-classical procedure used to obtain and interpret spectra of the chlorosome LH system is outlined in Chapter 3. In Chapter 4, spectral simulation results are presented and subjected to direct comparison against experimental data. Additional calculations for interpreting relevant spectral features are also shown in this chapter. Finally, Chapter 5 contains a brief analysis of the reliability of the theoretical and computational models employed in this project to provide reliable spectral calculations and conclusions regarding the origin of the spectral features in these LH systems.

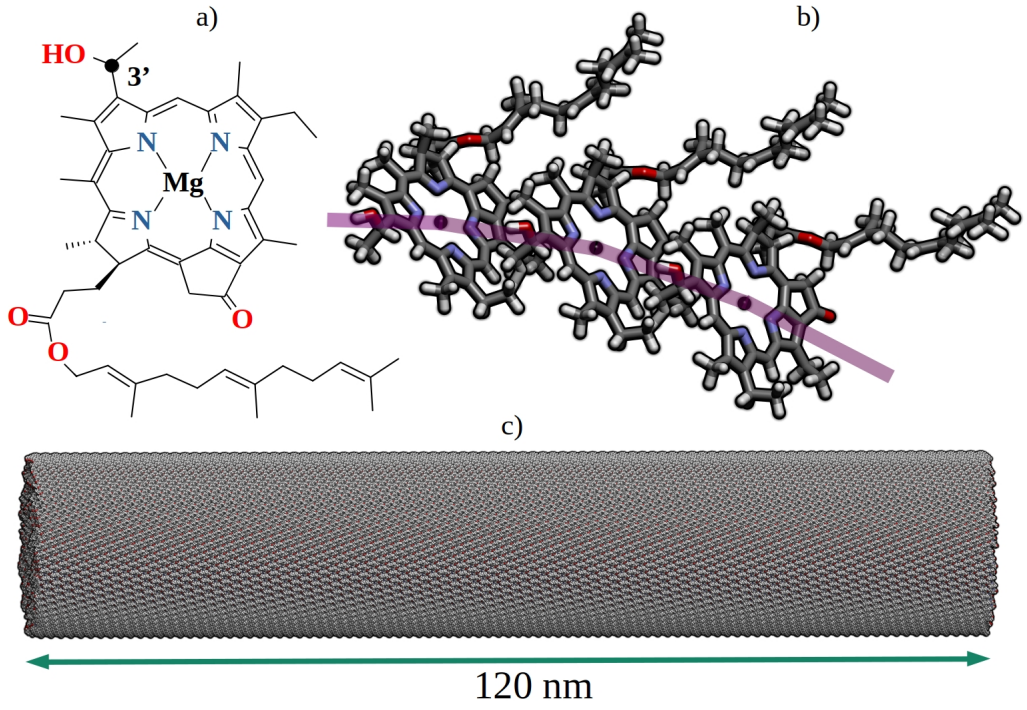

FIGURE 1.1: *a) Bacteriochlorophyll c (BChl c) structure. The pigment is in syn-conformation when the hydroxyl (OH) group at the **3'** carbon atom is at the same side as the wedged bond. If they are on opposite sides, the molecule is in anti-conformation. b) Syn-anti stack of BChlc pigments. c)Pre-assembled BChl tubular aggregate*

Chapter 2

Theoretical Framework

2.1 Collective excitations in molecular aggregates

A multichromophoric aggregate can be described through the Frenkel excitonic Hamiltonian as a set of N interacting two-level systems [7, 17]:

$$\hat{H}(t) = \sum_i \epsilon_i(t) b_i^\dagger b_i + \sum_{j \neq i} J_{ij} b_i^\dagger b_j - \sum_i \vec{\mu_i} \cdot \vec{E}(t)[b_i^\dagger + b_i] \tag{2.1}$$

Here, the site energy for corresponding to the excitation of the i_{th} is given by $\epsilon_i(t)$, with $b_i^\dagger$ and b_i as the Paulionic creation and annihilation operators respectively. The coupling strength of the i_{th} chromophore with the external electric field, $\vec{E}(t)$, is determined by the transition dipole $\vec{\mu}$.

The interaction between chromophoric units is accounted for through a pairwise coupling term J_{ij}. This is defined in terms of the (time-dependent) transition dipole moment $\mu(t)$ of the excitations localized in each chromophore and their Cartesian positions, in the so-called point-dipole coupling scheme [7, 17, 18]:

$$J_{ij}(\vec{\mu}_i(t), \vec{\mu}_j(t), R_{ij}(t)) = \frac{\vec{\mu}_i \cdot \vec{\mu}_j}{|R_{ij}|^3} - 3\frac{(\vec{\mu}_i \cdot R_{ij})(\vec{\mu}_j \cdot R_{ij})}{|R_{ij}|^5} \tag{2.2}$$

with i and j labeling the individual BChl pigments, while R stands for the distance between the i_{th} and j_{th} pigments.

The Hamiltonian in equation 2.1 presents a general form valid in principle for any arrangement of chromophores. However, to understand the nature of the excitonic eigenstates of the chlorosome, it is important to take into consideration the periodic symmetry

of the cylindrical system. In the limit of an infinitely large cylinder with a finite radius, the periodicity of the system allows the solutions of the Schrödinger equation of the system to be taken as plane waves modulated by a periodic function

$$\psi(r) = e^{ik \cdot r} u(r)$$

As will be seen below, formulation of the Frenkel Hamiltonian in the reciprocal space of a cylindrical geometry allows the convenient separation of the eigenstates of the cylinder into bands in the reciprocal space, which considerably simplifies the numerical effort of the problem, at a time that adds important general insight into the nature of the excitonic states in the system.

2.2 The Frenkel Hamiltonian for cylindrical ensembles

Consider a homogeneous aggregate of N identical molecules occupying a 2D lattice like that in Figure. Rolling the lattice in a certain direction defined by the chiral vector C, perpendicular to the main axis of a cylinder results in a stack of N_1 molecular rings, equally separated from each other by a distance h and occupied by a number N_2 of molecules at regular distances as shown in Figure 2.1.

Each ring is labeled as $n_1(1, 2, 3, ..., N_1)$. They are rotated relative to each other an helical angle γ, where $\vec{a}$ and $\vec{b}$ are the lattice vectors. This particular stacking yields a set of N_2 parallel helices on the surface of the cylinder, labeled as $n_2(1, 2, 3, ..., N_2)$. The total number of molecules in the cylinder is therefore $N = N_1 N_2$, and each chromophoric unit can be labeled in terms of the ring and chain aggregates as $n = (n_1, n_2)$ [7].

Since the present project deals with electronic transitions only, and all the chromophores are essentially equivalent, all the molecules in the cylinder are modeled as identical two-level systems, each of them with a defined transition dipole μ_n. In the homogeneous limit, these dipoles are equal in magnitude and orientation relative to the frame of the cylinder at the position of the molecule (See Figure 2.2).

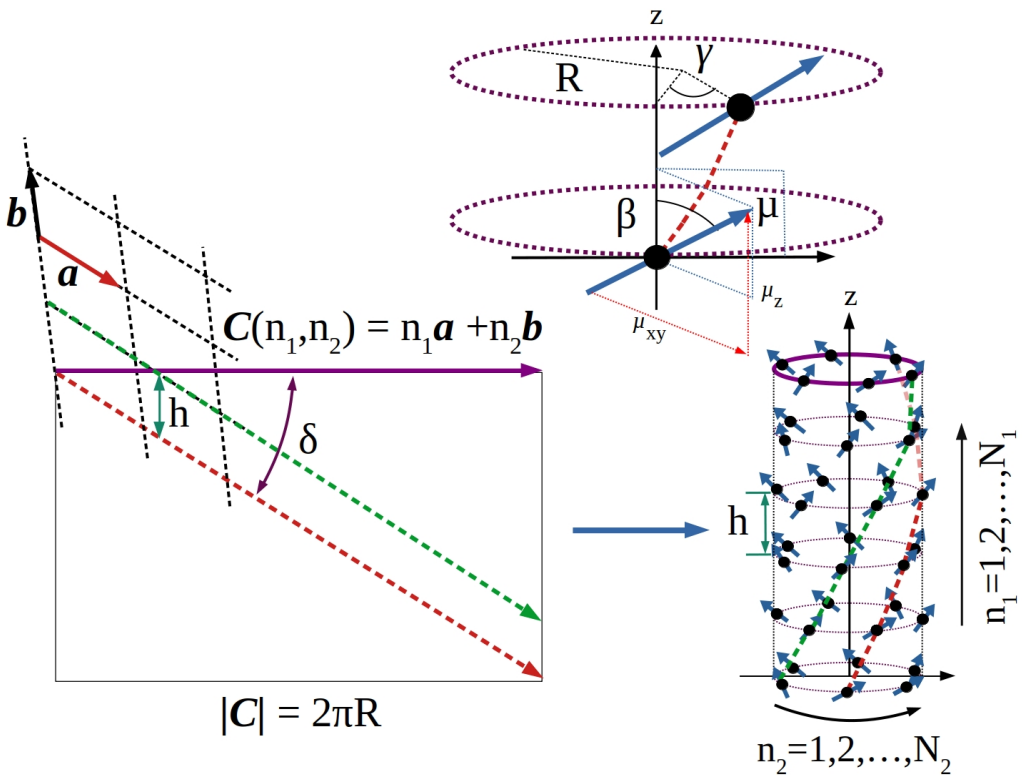

FIGURE 2.1: *Geometric description of a cylindrical molecular aggregate. The cylinder is obtained upon rolling of the lattice along the direction defined by the chiral vector C. The blue arrows indicate the transition dipoles μ of each pigment. They form an angle β with the cylinder main (z) axis. The aggregate is a stack of N_1 rings (labeled by n_1) rotated at an angle γ with respect to each other. Each of them contains N_2 molecules (labeled by n_2), yielding a set of N_2 parallel helices on the cylinder's surface exemplified by the dashed red and green curves.*

For simplicity, the electronically excited states of the system are described in absence of an external field. The the Hamiltonian in equation 2.1 can then be rewritten as

$$\hat{H}(t) = \sum_{n}^{N} \epsilon_n(t) b_n^\dagger b_n + \sum_{m \neq n} J_{nm} b_n^\dagger b_m \tag{2.3}$$

The coupling term J_{nm} between adjacent chromophoric units n and m is modeled using the point-dipole scheme of equation 2.2.

The eigenvectors $|k\rangle$ of the excitonic Hamiltonian, known as molecular excitons, are linear combinations of the site excitations:

$$|k\rangle = \sum_{n}^{N} c_n^k b_n^\dagger |g\rangle \tag{2.4}$$

Here $|g\rangle$ is the overall ground state (with all molecules in their ground state). The coefficients c_n^k reflect the participation of the n_{th} molecule in the k_{th} exciton state [19].

The cylindrical symmetry of the system dictates a Bloch form for the wave function for the wave functions along the ring direction (n_2). Thus before diagonalization of the Hamiltonian in equation 2.3, it is convenient to define a creation operator in the Bloch space for the states in the ring:

$$c_{n_1,k_2}^\dagger = \frac{1}{\sqrt{N_2}} \sum_{n_2} e^{ik_2\phi_2 n_2} b_n^\dagger \tag{2.5}$$

where $\phi_2 = \frac{\pi}{N_2}$. The wave number k_2 may take the values

$$k_2 = \begin{cases} 0 \quad \pm 1, \quad \pm 2, \quad ... \quad \pm\left(\frac{N_2}{2} - 1\right) & \text{for } N_2 \text{ even} \\ 0 \quad \pm 1, \quad \pm 2, \quad ... \quad \pm\left(\frac{N_2-1}{2}\right) & \text{for } N_2 \text{ odd} \end{cases} \tag{2.6}$$

corresponding with the states in the Bloch subspace of a ring aggregate [7].

It can be used to decouple the cylinder Hamiltonian into N_2 one-dimensional Hamiltonians characterized by the transverse wave number k_2.

$$\hat{H} = \sum_{k_2} \hat{H}(k_2) \tag{2.7}$$

Here, $\hat{H}(k_2)$ is the effective Hamiltonian coupling N_1 rings, each in its k_2 helical state in the reciprocal space defined as:

$$\hat{H}(k_2) = \sum_{n_1} \epsilon_{n_1,k_1}(t) c_{n_1,k_1}^\dagger c_{n_1,k_1} + \sum_{n1 \neq m_1} J(n_1 - m_1; k_2) c_{n_1,k_1}^\dagger c_{n_1,k_1} \tag{2.8}$$

The coupling term $J(n_1 - m_1; k_2)$ accounts for the interaction between adjacent rings at a defined state with momentum k_2 .

The coupling constant in the Bloch space can be obtained from its analogous in real space in equation 2.2 through the transformation

$$J(n_1; k_2) = \sum_{n_2} J(n_1, n_2) e^{-ik_2\phi_2 n_2} \tag{2.9}$$

In general, due to the helical nature of the system:

$$J(n_1, n_2) \neq J(n_1, -n_2) \tag{2.10}$$

and

$$J(-n_1; k_2) \neq J(n_1; k_2) \tag{2.11}$$

Therefore, the effective Hamiltonian $\hat{H}(k_2)$ is not inversion symmetric ($J(n) \neq J(-n)$) except for the state with $k_2 = 0$. For any other k_2 state:

$$\hat{H}(k_2) = \hat{H}(-k_2)^* \tag{2.12}$$

It means that the state $\psi_{k_1}(n_1)$ and its complex conjugated $\psi^*_{k_1}(n_1)$ are the n_1th component of the k_1th eigenvector of the Hamiltonians $\hat{H}(k_2)$ and $\hat{H}(-k_2)$ respectively, so these Hamiltonians share the same set of degenerated eigenvalues for any $k_2 \neq 0$ [7]. Considering also periodic conditions along the vertical axis of the cylinder, the total exciton state in the Bloch space, labeled $k = (k_1, k_2)$), can be written as:

$$|k\rangle = \sum_n \psi_k(n) b_n^\dagger |g\rangle \tag{2.13}$$

with

$$\psi_k(n) = \frac{1}{\sqrt{N}} e^{ik_2\psi_2 n_2} \psi_{k_1}(n_1; k_2) \text{ for } k_2 > 0 \tag{2.14}$$

$$\psi_k(n) = \frac{1}{\sqrt{N}} e^{ik_2\psi_2 n_2} \psi^*_{k_1}(n_1; -k_2) \text{ for } k_2 < 0 \tag{2.15}$$

From this definition, and considering only nearest-neighbor interactions, it follows that in the subspace of the ring direction only three states are required to describe the coupling between helical excitations, namely $k_2 = 0$ and $k_2 \pm 1$, since all the other states can be obtained from those. In the chain direction only the Bloch state $k_1 = 0$ is required to describe the excitation along the cylinder's major axis.

It follows that a cylindrical aggregate has 3 superradiant eigenstates : $(k_1 = 1, k_2 = 0)$, polarized along the axis of the cylinder, and the degenerate states $(k_1 = 1, k_2 \pm 1)$, both of them polarized perpendicular to the cylinder's axis [7]. Hereinafter, these states are simply denoted as $k = 0$ and $k = \pm 1$, respectively.

2.3 Order from Disorder

Thus far, only perfectly ordered aggregates have been considered. If the molecular disorder is neglected, the molecular excitons in equation 2.13 are delocalized along the whole cylindrical aggregate. This scenario is, of course, far away from the conditions of the interior of a bacteria. Thermal fluctuations, as well as inter and intra-molecular interactions, originate from position-dependent and time-dependent inhomogeneities in individual molecular transition energies and intermolecular couplings, described as static and dynamic disorders respectively [19]. Effects of disorder in excitonic systems include breaking of translational symmetry, mixing of homogeneous exciton states, and overall suppression of the delocalization of excitons [19–21].

Moreover, the selection rules shown in the previous section are only exact in the homogeneous limit. The presence of disorder breaks the selection rules to some extent, so more states become optically active, giving origin to bands of excitonic states with $k = 0$ and $k = \pm 1$ character [19].Therefore the inclusion of disorder effects in the Hamiltonian is essential for realistic simulations of light-harvesting systems in biological systems. In the present project, actual disorder taken from molecular conformations along MD trajectories has been included in the excitonic Hamiltonian in two ways:

1. **Diagonal disorder:** It is accounted for by correlated variations of the site energies, i.e, the diagonal elements of the Hamiltonian. It can be seen as a correction to the eigenenergies from their gas-phase value as a consequence of slightly different molecular surroundings. This energy shift in the excitation energy can be calculated by considering local interactions in a system composed of two subsystems namely, a central molecule and its surroundings. The interaction of the central chromophore with its environment will be different for its ground and excited states. Therefore, energy shift is calculated as the difference between the local energies of the ground and excited states of a reference molecule n [19].

$$\Delta\epsilon_n = \varepsilon_n^{(e)} - \varepsilon_n^{(g)} \tag{2.16}$$

The calculated shift has contributions from electrostatic (Coulombic) interactions ε^{el} and polarization interactions ε^{pol} between the central molecule and its surroundings. The coupling to a dynamical degree of freedom is accounted for by a fluctuating term shifting the molecular transition energies obtained by averaging over MD trajectories:

$$\varepsilon_n(t) = \epsilon_0 + \delta\epsilon_n(t) \tag{2.17}$$

The shift in the excitation energy $\delta\epsilon_n(t)$ is given by the Couloumbic intermolecular interactions at the position of the reference chromophore:

$$\delta\epsilon_n(t) = \sum_m^M \sum_l^L \frac{(q_m^e - q_m^g)q_l^g}{|\vec{R}_{ml}(t)|} \tag{2.18}$$

Here, the index m runs over the atoms in the the central molecule n, while l labels the remaining molecules. The ground state charge on the atoms of the molecules in the surroundings is denoted as q_l^q, while q_m^e and q_m^g denote ,respectively, the excited state and ground state charges on atoms of the reference molecule. $|\vec{R}_{ml}(t)|$ is the distance between atoms in the central and surrounding molecules.

The general excitonic Hamiltonian can then be written as:

$$\hat{H}(t) = \sum_n \varepsilon_n(t) b_n^\dagger b_n + \sum_{m \neq n} J_{nm} b_n^\dagger b_m \tag{2.19}$$

In this way, both, static and dynamic types of disorder are considered in the energy shift [19].

2. **Off-Diagonal disorder:** Also known as *interaction disorder*, accounts for the fluctuations in resonance interaction product of physical inhomogeneities in the cylindrical structure. It is included through equation 2.2 as variations into the electronic coupling between pigments, averaged over MD trajectories [11, 19].

Importantly, the natural chlorosome LH antennae are heterogeneous aggregates composed of several domains with different chemical composition and spatial arrangement, in multi-walled structures of tens of molecular cylinders [10]. This fact introduces a higher level of disorder, also refered to as mesoscopic disorder [22], that has not been considered in the present approach. Due to the molecular homogeneity of the aggregates, no static disorder related to chemical compositions and structural defects is included in this study.

2.4 Spectral Simulations

Computational simulation of spectra essentially consists of using the time evolution operator in NISE scheme [16, 23], solving the Schrödinger equation, and calculating the response function of the system interacting with a fixed set of external fields. These functions describe the time evolution of a statistical ensemble of quantum states under the effect of incident electric fields treated perturbatively. As with other perturbative approaches to light-matter interactions, the response functions can be diagrammatically represented using double-sided Feynman diagrams. More importantly, the Fourier transform of the response functions is used to calculate the line shape of the spectra [24]. In the reminder of these section, the NISE mathematical formalism is described altogether with the expression used to simulate the spectra.

2.4.1 Numerical Integration of the Schrödinger Equation

The time-evolution of a quantum-mechanical system is described by the time-dependent Schrödinger Equation:

$$\frac{\partial}{\partial t}|\psi(r,t)\rangle = -\frac{i}{\hbar}\hat{H}|\psi(r,t)\rangle \tag{2.20}$$

To keep notation to a minimum, in the following discussion the spatial dependence of wave function will not be explicitly shown.

By expanding the system wave function in terms of the sites basis $\{\phi\}$, equation 2.20 can be rewritten in matrix form:

$$\frac{\partial}{\partial t}\mathbf{c}(t) = -\frac{i}{\hbar}\hat{H}\mathbf{c}(t) \tag{2.21}$$

with $\mathbf{c}$ denoting the matrix of expansion coefficients. An analytical solution might be hard to obtain, especially for large systems like the chlorosome. For numerical integration of this equation using small time increments, the Hamiltonian is treated as constant during each integration step. The integration over one such time step Δt yields:

$$c((n+1)\Delta t) = e^{\left(-\frac{i}{\hbar}\right)\hat{H}(n\Delta t)\Delta t}c(n\Delta t) \equiv U((n+1)\Delta t, n\Delta t)c(n\Delta t) \tag{2.22}$$

In this approach, the time-evolution operator $U$for an arbitrary number of consecutive n time steps can be found through a time-ordered product operation from the left with increasing m:

$$U(n\Delta t, 0) = \prod_{m=1}^{m=n} U(m\Delta t, (m-1)\Delta t) \tag{2.23}$$

It can be seen as a propagator acting on the wave function and thereby propagating the system forward in time [25]. Notice that the last expression depends only on the time interval $(m\Delta t, (m-1)\Delta t)$ while $\hat{H}$ is assumed to be time-independent. In practice, some further approximations can be made so that the time-dependent Excitonic Hamiltonian in equation 2.1 can be fitted into the NISE scheme.

2.4.2 Linear Absorption

In the NISE approach, the absorption spectrum of a system interacting with a linear polarized field of frequency ω is given by

$$I(\omega) = \int_0^\infty dt \sum_{\alpha=x,y,z} \langle\langle g|\mu_\alpha(t+t_0)U(t+t_0,t_0)\vec{\mu}_\alpha(t_0)|g\rangle\rangle e^{-i\omega t} \tag{2.24}$$

The outer brackets denote the ensemble average over different starting points (t_0) along the Hamiltonian trajectory, and the subscript α on the transition dipole shows the Cartesian component of the vector [25].

2.4.3 Linear Dichroism

In linear dichroism spectra, the difference in absorption spectrum for two beams of linearly polarized light of which the polarization vectors are mutually perpendicular is measured for a sample where the intrinsic structures are aligned [25].

The LD is then given by

$$LD(\omega) = I_\parallel(\omega) - I_\perp(\omega) \tag{2.25}$$

$I_\parallel(\omega)$ and $I_\perp(\omega)$ are the absorption spectra for light polarized respectively parallel and perpendicular to an arbitrary axis. They are calculated using equation 2.24.

2.4.4 Two-Dimensional Electron Spectroscopy (2DES)

During the 2DES experiment, 3 laser pulses with the same frequency ω are applied to the sample at different time delays. The corresponding signals are collected in two-phase

matching conditions: rephasing diagrams in the $\vec{k}_I = -k_1 + k_2 + k_3$ direction, and non-rephasing diagrams are in the $\vec{k}_{II} = +k_1 - k_2 + k_3$ direction, where k_1, k_2, and k_3 are the wave vectors of the incoming fields. Each of these signals contains the contributions of three optical processes, namely ground state bleaching (GB), stimulated emission (SE), and excited state absorption (EA) [24, 25].

The overall 2DES signals are converted to the frequency domain using 2D Fourier transforms [24]. This process results in the following expressions for rephasing (I) and non-rephasing (II) conditions:

$$I^{(I)}(\omega_3, t_2, \omega_1) = \int_0^\infty \int_0^\infty d_{t_3} d_{t_1} (S^{(I)}_{GB}(t_3, t_2, t_2) + S^{(I)}_{SE}(t_3, t_2, t_2) + S^{(I)}_{EA}(t_3, t_2, t_2)) e^{i(\omega_3 t_3 + \omega_1 t_1)} \tag{2.26}$$

and

$$I^{(II)}(\omega_3, t_2, \omega_1) = \int_0^\infty \int_0^\infty d_{t_3} d_{t_1} (S^{(II)}_{GB}(t_3, t_2, t_2) + S^{(II)}_{SE}(t_3, t_2, t_2) + S^{(II)}_{EA}(t_3, t_2, t_2)) e^{i(\omega_3 t_3 - \omega_1 t_1)} \tag{2.27}$$

Here t_2 is the population time, while the S terms are the response functions corresponding to GB, SE, and EA processes. The expressions of response functions for the spectroscopic techniques used in this project can be found in various textbooks [24, 25]. The 2DES correlation spectrum is then calculated as the imaginary part of the sum of the rephasing and non-rephasing signals:

$$I_{2DES}(\omega_3, t_2, \omega_1) = Im(I^{(I)}(\omega_3, t_2, \omega_1) + I^{(II)}(\omega_3, t_2, \omega_1)) \tag{2.28}$$

Essentially, 2DES provides correlation maps between excitation and probing frequencies. If the system is excited during the first time delay and probed during the third time delay, the signal observed corresponds to the system at a point in the spectrum connected with the frequency ω_1 it had during the first delay and the frequency ω_3 it had during the third time delay along. The system's evolution during the waiting time t_2 determines the correlation between incident and probing frequencies [24, 26]. The double-sided Feynman diagrams in Figure 2.2 illustrate the density matrix's evolution during the system's interaction with three laser pulses.The letter change during these times indicates the possibility for the quantum state to change due to the mixing of states, produced by thermal

fluctuations of the system. Such a change can be produced either by coherence transfer or population transfer, depending on whether the change occurs during coherence (t_1,t_3 or population (t_2) times. [27, 28].

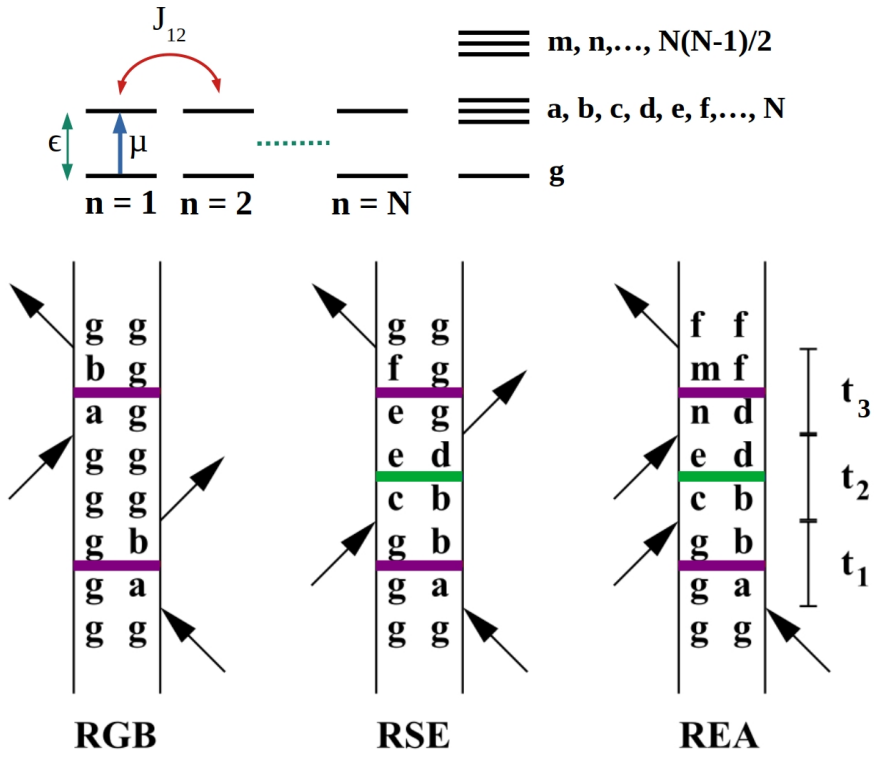

FIGURE 2.2: *Top: N two-level systems interacting through a pairwise coupling term J. Different single excited states are labeled with (a-f), while (n,m) label double excited states. The ground state is represented by g. Bottom: Double-sided Feynman diagrams for GB, SE, and EA processes. The purple lines indicate potential population transfer, while the green lines indicate potential coherence transfer. The mixing of states during coherence and population times is explicitly shown. Only diagrams for rephasing conditions are shown for simplicity.*

Chapter 3

Methods

3.1 Initial structure

The structures employed in this work were based on the bchR mutant of *Chorobaculm tepidum*, composed essentially of BChl *c* pigments, resulting in more homogeneous structures that allow for detailed theoretical modeling of the spectra. As mentioned in the introduction, a single-molecule spectroscopy study on bchR mutant chlorosomes determined an average angle $\beta \approx 55°$ from the ratio of parallel and perpendicular oscillator strengths [10]. It coincides with a structure with chirality of $\delta \approx 112°$, in alignment with previous computational studies regarding the thermodynamic stabilities of BChl *c* assemblies [5]. The same study also reports another thermodynamically stable structure with $\delta \approx 50$. A straightforward analysis of the average angle β of the BChl showed that this structure conveniently led to $\beta \approx 0$.

In order to determine the contribution of the $k = \pm 1$ and $k = 0$ excitonic bands at different chiralities in the spectral features of the chlorosome LH, two structures with chiralities $\delta \approx 112°$ and $\delta \approx 50°$ were build (See Figure 1.1). Individual tubes of 120 nm long were created for fixed δ angles and cylinder radius R using the software CtubeGen [29]. The data were post-processed to generate the triple-tube structures shown in Figure 3.1. Refer to the literature for more detail on this general procedure [11]. For the results to be comparable between these two aggregates, the computational process described in the upcoming sections was applied exactly in the same way for both systems.

Importantly, different δ lead to cylinders with slightly different radii. Consequently, the inter-cylinder distance reported from cryo-EM experiments was only achieved for aggregate $B\delta \approx 50°$. However, in both cases, this separation length was kept within an experimental

value of $\sim 2-3$ $\mathring{A}$ [4, 11].

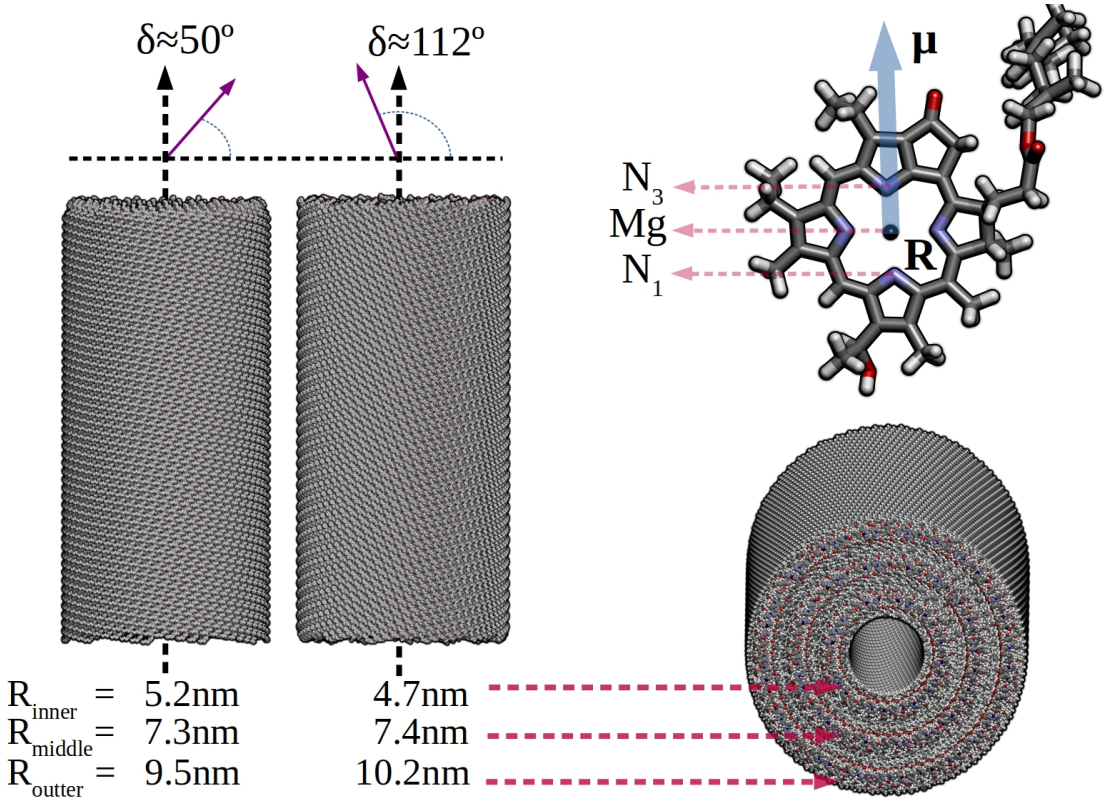

FIGURE 3.1: *Left: Triple tube initial structures for aggregates* $\delta \approx 112°$ *and* $\delta \approx 50°$. *Bottom-right: transversal cut of triple-walled BCHl nanotube. Top-right: Graphical representation of transition dipole* μ *in BChl molecule, with its origin at the Mg atom position* R

3.2 Molecular Dynamics

NVT all-atom MD simulations were conducted to obtain nuclear coordinates of the system along a time trajectory of 10 ps. The simulations were carried out using the Gromacs software [30] (version 2016.1) and the OPLS-AA force field [31, 32]. All simulations were performed with periodic boundary conditions along all dimensions. Steepest descent optimization and equilibration MD simulations of 1 ns were performed prior to production simulations to avoid nonphysical atomic overlap and ensure stable MD simulations. Production MD simulations were performed at 300 K with the velocity-rescaling thermostat [33] maintaining the temperature. Five hundred-one snapshots of the nuclear coordinates were

collected every 20 fs along the MD trajectory. Further spectra calculations using the NISE scheme require that the Hamiltonian can be considered constant during each time interval. For this purpose, the $\mu(t)$ and $R(t)$ information extracted from MD simulations with a 20 fs time-step was modified to fit a shorter time-step of 4 fs. The transformation was carried out using a Python script that artificially shortened the time step by increasing the number of intermediate steps in which energy is the same during the whole interval, yielding a total of 2005 snapshots. The coordinates along the new trajectory were used to calculate time-dependent information of the transition dipole vectors $\mu(t)$, like their spatial orientation and positions $R(t)$. The unitary transition dipole moment is given by the vector connecting the two indicated Nitrogen atoms in Figure 3.1, with the origin given by the coordinates $R(t)$ of the Mg atom. Experimentally, this vector's magnitude has been estimated as 5.48 D for BChl *c* in methanol solution [11, 34].

3.3 Parametrization of the Excitonic Hamiltonian

Once $\mu(t)$ and $R(t)$ have been extracted from the MD trajectory, the Frenkel Hamiltonian is calculated using the equation 2.1. The Hamiltonian is a 2D matrix composed of diagonal (site energy) and off-diagonal (electronic coupling) terms. These matrix elements fluctuate due to the thermal bath dynamics effect on the excitation frequencies of the individual chromophores and the coupling strength between them. Disorder effects were introduced in the site energies (diagonal terms) as described in subsection 2.3 around the lowest and bright excitation (Q_y) energy of a BChl c pigment molecule in methanol, $\nu = 15390$ cm^{-1} [35]. The off-diagonal terms, i.e., the electronic couplings J_{ij} between chromophores, are calculated via the standard point-dipole approximation (PDA) in equation 2.2. The PDA is the simplest approximation for couplings between different states, and it is accurate when the distance between the chromophores is larger than their size [1, 18]. Further extensions to include charge transfer and transition multipole effects in the coupling are also possible. They are generally based on transition densities of the interacting BChls calculated with time-dependent density functional theory (TD-DFT) [1, 13]. However, electronic structure calculations can become time-consuming for large systems, even if cheap semi-empirical methods are employed. On the other hand, only three atoms per chromophore are relevant for the electronic coupling terms within the PDA scheme making it an appropriate approach for the simulation of LH complexes of realistic size.

3.4 NISE calculations

The parametrized Hamiltonians are employed in the NISE approach to calculate the different spectra using the NISE software [14–16, 23]. Details on the calculations performed for this project are explained below.

3.4.1 Linear Spectra simulations

Linear absorption and linear dichroism spectra were readily calculate with NISE based on equations 2.24 and 2.25, respectively. Coherence times, t_1 and t_3, the population time were set to arbitrary values since they are not used in linear spectra. The input Hamiltonians for systems were built based on initial structures with 27829 BChl molecules for aggregate with $\delta \approx 112^\circ$ and 27675 for aggregate with $\delta \approx 50^\circ$.

Linear spectra combination

The LD spectrum can be further combined with the absorption spectrum. It allows the explicit separation of peaks with different symmetries as follows:

$$\frac{1}{3}(I + 2LD) = \mu_z^2 \tag{3.1}$$

$$\frac{1}{3}(I - LD) = \frac{1}{2}(\mu_x^2 + \mu_y^2) \tag{3.2}$$

Here $\mu_{\alpha=x,y,z}$ are the Cartesian components of the transition dipole moment of the excitonic states. Equation 3.1 corresponds to eigenstates with the transition dipole parallel to the tube axis, while equation 3.2 corresponds to eigenstates with the transition dipole perpendicular to the tube axis.

3.4.2 Two-Dimensional Electron Spectroscopy (2DES)

2DES spectra were calculated using the expressions in 2.27 and 2.28 within the NISE scheme. Since calculating the third-order optical response is computationally expensive, a single-walled tube of 350 nm long (one for each δ angle) was cut out from the middle tube in the original triple-tube arrangement. A new Hamiltonian was built using the original triple-tube Hamiltonian data for the atoms in this smaller system. For the spectral simulations,

the coherence times (t_1 and t_3) were fixed at 256 fs. The waiting times t_2 varied from 0 fs to 400 fs in steps of $\sim$ 25 fs. By default, NISE calculated the 2DES for three different polarization setups: parallel, perpendicular, and cross-polarization. Simulations were set up so that the reference axis for the polarization direction coincides with the cylinder's major axis, i.e., the Cartesian z-axis.

Polarization sequences

Specific polarization sequence directions have been used to probe the molecular configuration (orientation and magnitude) of the transition dipole moments [36] and enhance various features in 2DES [37]. Three different polarization schemes have been used in this project, namely all-parallel, all-perpendicular, and cross-polarized. The all-parallel spectra were calculated assuming a sequence of pulses in the directions (0°, 0°, 0°, 0°) polarization sequence. Similarly, the all-perpendicular spectra arose from the (90°, 90°, 90°, 90°). In both cases, GB and the combined SE+EA processes contribute equal footage to the total 2DES signals. Their intensities are expected to vary depending on the component of the transition dipole moment enhanced by the polarization sequence [38].

The cross-polarized scheme, given by the sequence of pulses in the directions (45°, -45°, 90°, 0°) is thought to eliminate all diagonal peaks, leaving only cross-peaks in the spectra, therefore enhancing the coherences between the ground and excited states [38]. Given this capability, the cross-polarized scheme seems as a suitable technique for studying the dynamics of excited states in molecular aggregates. However, the presence of disorder strongly affects the complexity of alternating signs in the signal, making interpreting these spectra rather difficult. Besides, only the all-parallel 2DES polarization experimental data is usually available. In this regard, computational spectroscopy simulations are powerful tools for spectra interpretation. Indeed, polarization-controlled 2DES techniques, supported by theoretical modeling have been employed to study coherence dynamics in the FMO complex of green sulfur bacteria [39] and the LH2 complex of purple bacteria [27]. The origin of particular features in the simulated cross-polarized 2DES found in this work was further studied by decomposing the full cross-polarized spectra into their individual GB, SE, and EA contributions.

Anisotropy decay calculation

2DES spectra at different polarization conditions can be combined to extract useful data related to the relative orientation of transition dipole moments. In particular, the anisotropy

decay measures the loss of the orientational correlation of the transition dipole connected with the underlying transitions [27]. It can be obtained from the simulated/experimental signal in the all-parallel($\parallel$) and all-perpendicular ($\perp$) polarization configurations as a function of the population time t_2. A value of 0.4 indicates a perfect correlation [24, 38].

$$r(t_2) = \frac{I_{\parallel}(t_2) - I_{\perp}(t_2)}{I_{\parallel}(t_2) + 2I_{\perp}(t_2)} \tag{3.3}$$

Chapter 4

Results

4.1 Linear spectra simulation

Figure 4.1 shows the simulated UV-vis absorption spectra for aggregates with $\delta \approx 112°$ and $\delta \approx 50°$. The experimental data recorded for the WT chlorosome is also included for comparison. The excitonic parameters of the three spectra are summarized in Table 4.1. The mismatch between experimental and predicted absorption peaks might arise from many factors, including the selected vacuum energy values for the site energies (refer to section 3.3 for details) and the neglect of molecular heterogeneity and mesoscopic disorder in the multiscale model [22]. However, since the former is an arbitrary value, and higher levels of the disorder are not a matter of interest in this study, the peak position does not change the following interpretation.

The chirality of aggregate with $\delta \approx 50°$ renders a $\beta \approx 0°$. Hence, the perpendicular component of the overall transition dipole vector is neglectable, and the superradiant non-degenerate states in the $k = 0$ band dominate the absorption spectrum. On the other hand, the $\delta \approx 12°$ aggregate is expected to have an appreciable contribution of $k = \pm 1$ states in its spectrum due to the larger μ_x and μ_y components ($\beta \approx 55°$). As appreciated in Figure 4.1, the FWHM of aggregate w with $\delta \approx 112°$ is in better agreement with the experimental spectrum than aggregate with $\delta \approx 50°$. It aligns with the results from single-molecule spectroscopy measurements that report transition dipole moments oriented with $\approx 55°$, further supporting the dominance of the structure with a macroscopic chirality $\approx 112°$. Despite the simplifications of the model, the resultant spectra show that the excitonic Hamiltonian in a multiscale approach accounts for an accurate system's description. Other system features like charge transfer effects, higher levels of disorder, or intermolecular vibration

effects may also lead to narrowing or broadening of the spectra. However, including such effects in a multiscale approach is out of this project's scope.

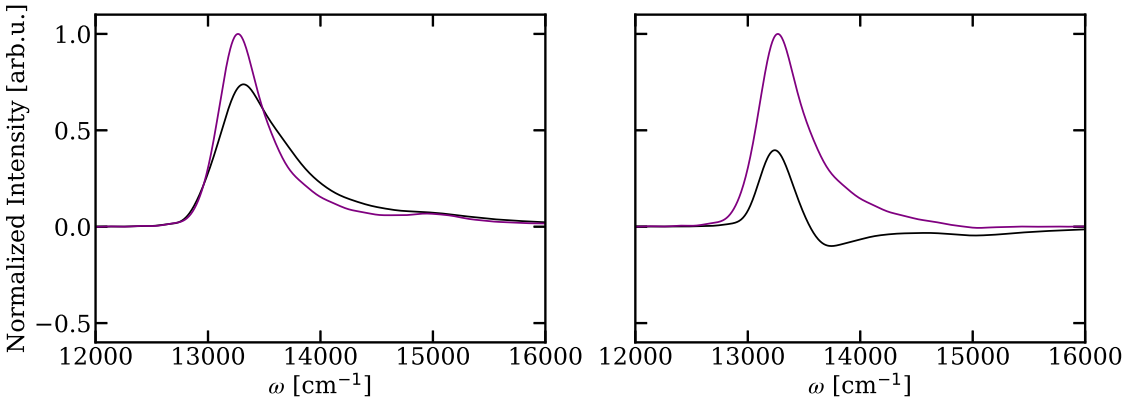

FIGURE 4.1: *Simulated linear spectra for aggregates $\delta \approx 112°$ (black) and $\delta \approx 50°$ (purple). Linear absorption (left) and linear dichroism(right) are normalized with respect to corresponding maxima. The positions of the spectra have been shifted to match the frequency at the peak position of experimental spectrum*

System	**FWHM** [cm^{-1}]	**Max. Frequency** [cm^{-1}]
$\delta \approx 112°$	724.78	14645
$\delta \approx 50°$	492.69	14597
Exp	801.79	13315

TABLE 4.1: *Linear absorption excitonic data for simulations of aggregates A and B, against experimental values [9]*

The difference between the optical response of structures with $\delta \approx 112°$ and $\delta \approx 50°$ is even more evident when analyzing the LD spectra on the right side of Figure 4.1. The position of the peak and the left-side tail match smoothly between spectra of $\delta \approx 112°$ and $\delta \approx 50°$ aggregates, indicating the presence of a common band of superradiant $k = 0$-like states oriented parallel to the cylinder's main axis. In addition, aggregate with $\delta \approx 112°$ displays a broad feature whose area is comparable to the main peak. It indicates the presence of a second orientational contributor to the LD spectrum, which is oriented perpendicular to the cylinder axis. This feature is absent in the LD spectra of aggregate

$\delta \approx 50°$), demonstrating the presence of a single orientational component of its transition dipole moment and the total absence of $k = \pm 1$-like states when the chirality is changed.

The time-dependent distribution of the orientation of the TDMs eventually mixes up the degenerate and non-degenerate states in a single band centered around the frequency at the peak of the non-degenerate $k = 0$ band. Therefore, the degenerate states in the $k = \pm 1$ bands are not experimentally "visible" when using linear absorption. However, it is still possible to fully identify the perpendicular and parallel components of the absorption spectra through the combination of the linear absorption and LD spectra, as shown in subsection 3.4.1.

As seen in Figure 4.2, the spectrum associated with the parallel component of the dipole vector, μ_z for the $\delta \approx 50°$ aggregate matches almost perfectly with the one of its homologous with $\mu_z A$, demonstrating that this signal arises from the non-degenerate states in the $k_2 = 0$ band for both aggregates. As expected, the signal corresponding to the perpendicular-oriented dipole $\mu_{xy} B$ is very weak. On the other hand, its counterpart in aggregate $\delta \approx 112°$ originates a broad band whose intensity is comparable to the signal of the parallel-oriented dipole. This band largely accounts for the recovery of the experimental FWHM. Since the chemical composition of both aggregates is essentially the same, the differences between their linear spectra indicate that macroscopic chirality dictates the orientation of TDMs within the cylinder.

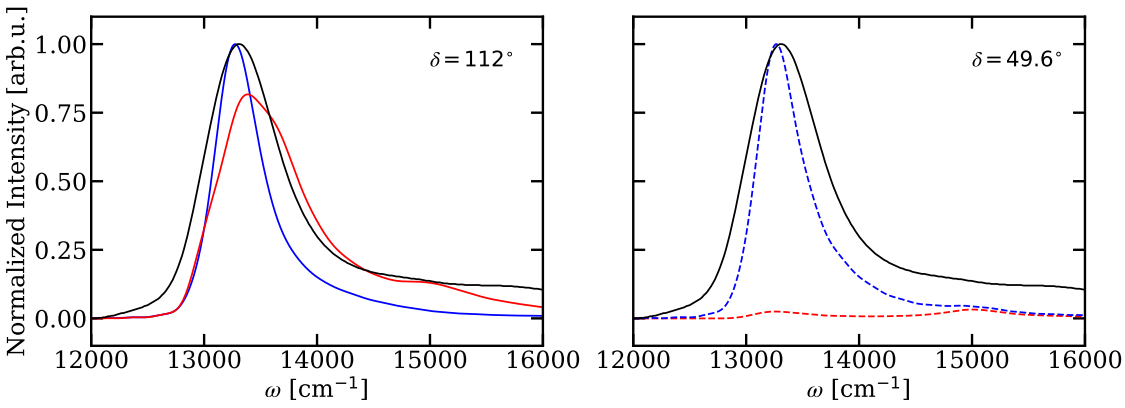

FIGURE 4.2: *Mathematical decomposition of the absorption spectra. Left side: (blue) parallel polarized component and (red) parallel polarized component of aggregate $\delta \approx 112°$. Right side: (dashed-blue) parallel polarized component and (dashed-red) perpendicular polarized component of aggregate $\delta \approx 50°$. Normalized experimental spectrum is shown in black for comparison*

4.2 2DES simulations

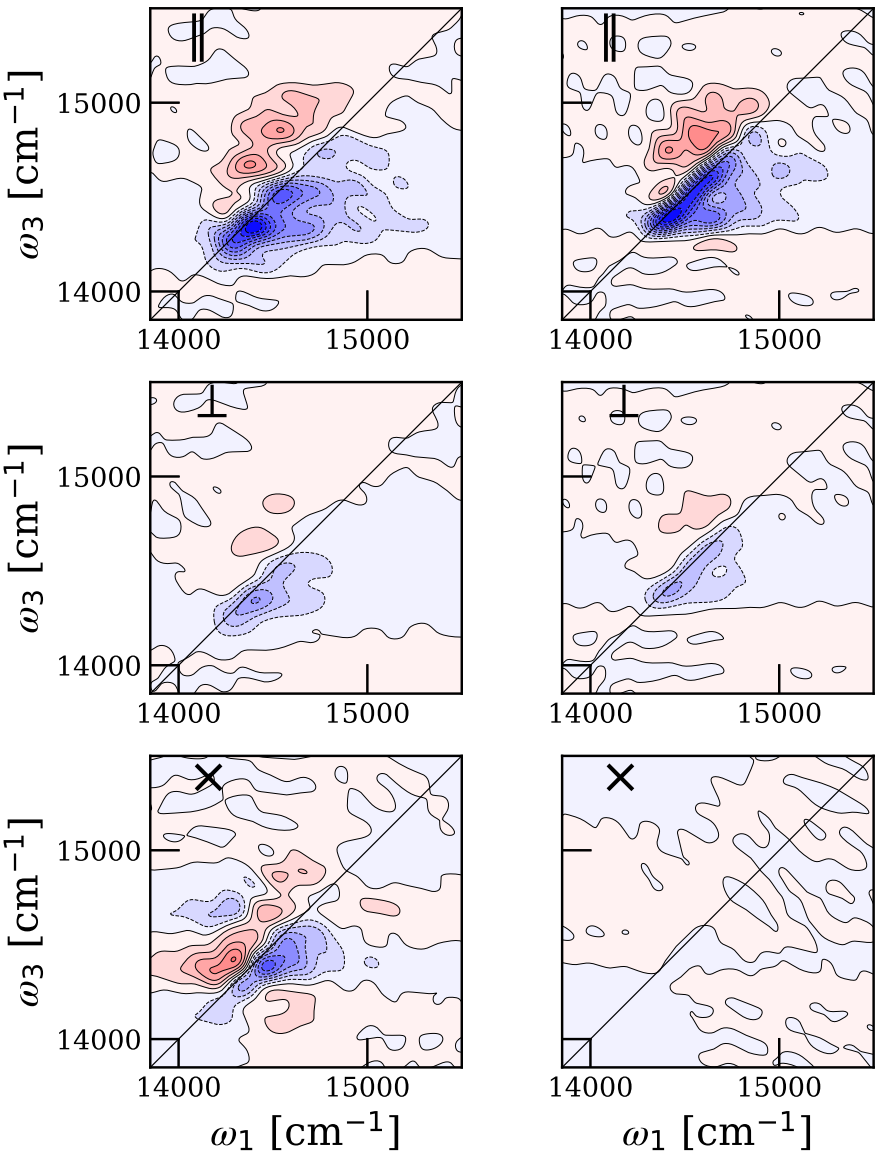

FIGURE 4.3: *2DES spectra at $t_2 = 0$ for parallel (∥,top), perpendicular (⊥, middle), and cross (×, bottom) polarization of aggregates $\delta \approx 112°$ (left column) and $\delta \approx 50°$ (right column). Red contours represent the absorption signal. Blue contours represent bleach.*

Figure 4.3 shows the parallel, perpendicular, and cross-polarized 2DES spectra at zero population time for both aggregates. All the plots were scaled to the point with max intensity at $t_2 = 0$ time obtained with parallel sequence. The cross-polarized signal is multiplied

by 5 for comparability. The peak shapes and positions are similar in both aggregates' parallel and perpendicular-polarized spectra. The peak shapes and positions are similar in both aggregates' parallel and perpendicular-polarized spectra at $t_2 = 0$. As expected, the signal obtained using a perpendicular pulse sequence is weaker for aggregate $\delta \approx 50°$ ($\beta \approx 0°$). Since no experimental data is available for perpendicular and cross-polarized spectra, the matching between experimental and theoretically predicted spectral trends in the parallel-oriented spectrum highlights the accuracy of the approach and validates the theoretical model for further simulations.

In contrast, the cross-polarized spectra in Figure 4.3 present several discrepancies appreciable at first sight. The cross-polarization scheme was meant to eliminate the diagonal peaks and reveal the cross-peaks, often obscured by the diagonal features.The coherences between the ground and first excited states are indeed appreciable in the cross-polarized spectra of aggregate $\delta \approx 112°$. However, a persistent peak is observed close to the diagonal, even when the polarization scheme should have suppressed it. On the other hand, the bad signal-to-noise ratio in cross-polarized spectra of $\delta \approx 50°$, provoked by the low intensity of the signal, makes it difficult to distinguish structural features from background noise.

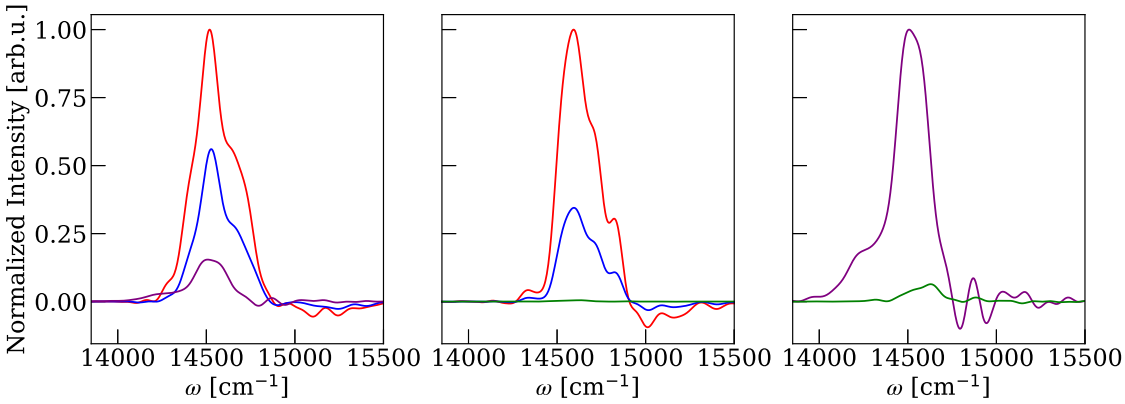

FIGURE 4.4: *Diagonal cuts of the 2DES spectra at $t_2 = 300fs$. Red: Parallel-polarized. Blue: Perpendicular. Purple: Cross-polarized of Aggregate $\delta \approx 112°$. Purple: Cross-polarized of Aggregate $\delta \approx 50°$. Left: Aggregate $\delta \approx 112°$. Middle: Aggregate $\delta \approx 50°$. Right: Comparison of diagonal cuts of cross-polarized spectra for both aggregates*

The diagonal cuts of the different polarized 2DES at the position of the peak in the parallel-polarized spectra are shown in Figure 4.4 for $t_2 = 300$fs. As expected, the normalized intensity of the perpendicular-polarized spectrum is about one-third of the parallel-polarized one for aggregate $\delta \approx 50°$. This ratio is increased to around one-half when going

to aggregate $\delta \approx 112°$ due to larger perpendicular components of the system's TDMs. The difference of almost two orders of magnitude between intensities of the cross-polarized spectra $\delta \approx 112°$ and $\delta \approx 50°$ is a more interesting feature. It suggests that the spectral feature found in the cross-polarized 2DES is not only unexpected but also its intensity seems to depend strongly on the chirality of the system.

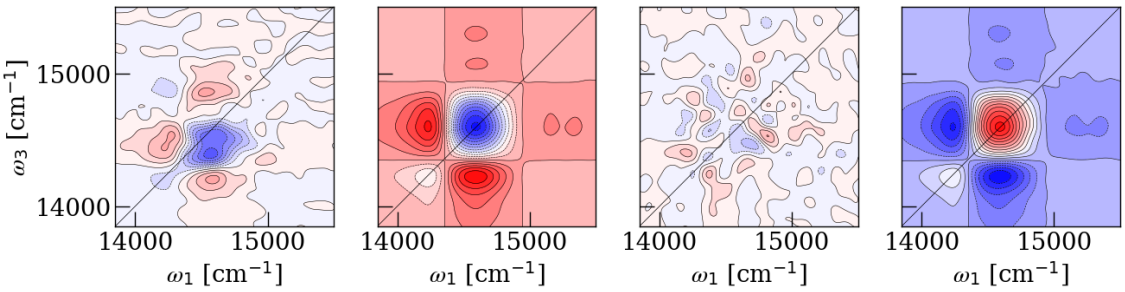

FIGURE 4.5: *Decomposition of the 2DES cross-polarization spectra of $\delta \approx 112°$ at $t_2 = 300fs$. From left to right: Full 2DES spectrum, GB, SE,and EA spectra*

The 2DES cross-polarized spectrum at 300 fs was decomposed in the GB, SE, and EA contributions, as shown in Figure 4.5, to gain insight into the origin of the unexpected diagonal peak. The cross-polarization sequence was selected to eliminate the ground state bleaching signal and emphasize all dipole pairs with orthogonal orientation [38,40]. Therefore, the diagonal peak in the cross-polarized spectra was expected to arise from electronic coherences in SE or EA processes. However, while the SE signal is not further distinguishable from the numerical noise after 300 fs, the diagonal feature is still present in the full cross-polarization spectra. It rules out that the peak does originate from an electronic coherence between two degenerate states. Even though the EA still has a considerable absorptive contribution at the location of the persistent peak feature at $t_2 = 300fs$, the GB signal seems to dominate the spectrum. Additional spectra calculations at larger t_2 (400 and 1000 fs) confirm that the shape of GB and EA signals are not further changing, and their intensities decay with the electronic excitation's lifetime.

The time evolution of the intensities for the spectral components at the position of the cross-polarized peak in Figure 4.6 confirms that the electronic coherences of SE and EA signals have a relevant contribution at very early times only. The EA signal rapidly decays to intensity values comparable to the magnitude of the GB, while the SE intensity goes close to zero after 72 fs. The GB signal is essentially flat throughout the trajectory but never zero. Indeed, oscillatory behavior related to vibrational coherences is observed in the

GB signal. Moreover, after a population time of 48 fs, the GB dominates over the other contributions to the full signal cross-polarized spectra. The difference between the GB and EA intensities is small, $\sim 10^{-2}$, but it is enough to avoid the suppression of the GB signal reminder time trajectory. The lack of cancelation yields negative bleaching intensities for the cross-polarized signal, as seen on the right side of Figure 4.6. It indicates that the peak in the cross-polarized spectrum arises essentially from the ground state bleaching processes.

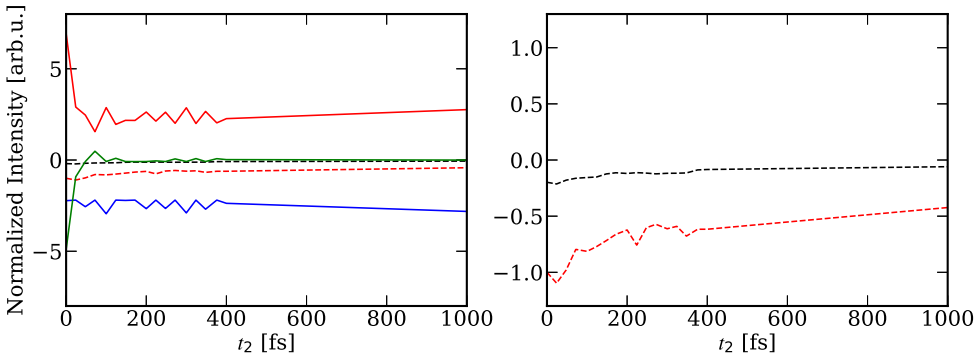

FIGURE 4.6: *Time evolution of spectral components' intensities of* $\delta \approx 112°$. *Left: SE (Green), EA (Red) and GB (blue) intensities at the position of the cross-polarized peak* ($t_2 = 300$ *fs). Full cross-polarization and parallel-polarized are shown in dashed-black and red respectively. Right: Zoom in to cross and parallel polarized signals. All intensities are plotted relative to the parallel signal intensity at the position of the cross-polarized peak* ($t_2 = 0$ *fs)*

In principle, no ground-state bleach signal should be present as the identity of the excited states is maintained during the coherence times in the cross-polarized experiment [41]. However, the disorder could break the system's degeneracy allowing the mix of the $k = \pm 1$ states through a coherence transfer process during the coherence times. Such a process would imply a fast decay in anisotropy due to the loss of orientational correlation of the transition dipole connected with the underlying transitions [38, 41].

The time-evolution of the anisotropy, measured at the respective cross-polarized peaks for aggregates $\delta \approx 112°$ and $\delta \approx 50°$, is shown in Figure 4.7. The anisotropy curve for $\delta \approx 112°$ decays from 0.4 to 0.1, reflecting the loss of orientational identity of the $k = \pm 1$ states and coherence transfer in a 400 fs time scale.

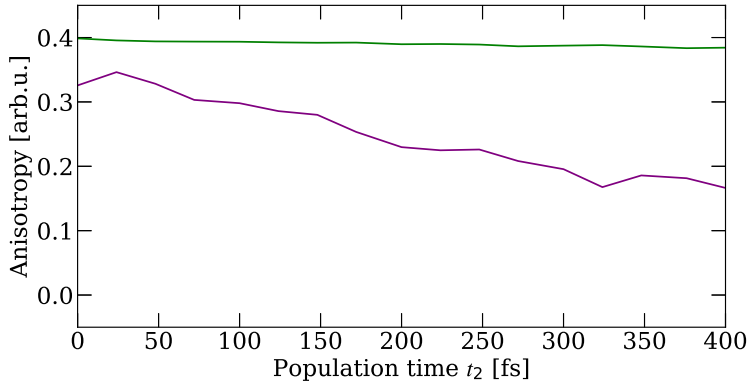

FIGURE 4.7: *Anisotropy decay as a function of population time t_2 for aggregate $\delta \approx 112°$ (purple) and $\delta \approx 50°$ (green) at the position of their corresponding parallel-polarized peaks*

From linear spectroscopy analysis in the previous section, it is known that aggregate B presents an almost total lack of a perpendicular component of the transition dipole. Therefore, the anisotropy decay in aggregate B can only come from the non-degenerate $k = 0$ state. Any mixing with $k = \pm 1$ will be neglectable small due to the reduced magnitude of the perpendicular component of the transition dipoles. It boils down to a slow anisotropy decay seen in Figure 4.7, indicating that the transition dipole associated with the eigenstates of this system are maintaining their orientational identities, and no significant coherence transfer occurs during the same time scale.

4.3 Discussion

The cross-polarized feature in aggregate $\delta \approx 112°$ has been attributed to a coherence transfer process between the two $k = \pm 1$ states during the t_1 and t_3 time periods. A coherence may initially be generated between, for example, the ground state and a singly excited state a. However, the coherence transfer originated from the bath-induced mixing of quantum states in the system may lead to coherence between the ground state and the state b if the excited states are close in energy (See Figure 2.2). In the cylindrical ensemble, the degeneracy of the states in the $k = \pm 1$ band is lifted by molecular disorder, allowing states with different polarization directions (k_y and k_x) to mix. The coherences between the ground state and the degeneracy-lifted states enhance the bleaching signal bypassing the GB signal suppression.

The calculation of the polarization anisotropy for both aggregates confirmed this sce-

nario. Fast time decay in the anisotropy of aggregate $\delta \approx 112°$ was observed, indicating the loss of orientational identity of the $k = \pm 1$, initially oriented orthogonal to each other, as the mixing between states by coherence transfer occurs in an ultrafast time scale. For aggregate $\delta \approx 50°$, the magnitudes of the μ_x and μ_y components were too small to allow efficient non-adiabatic mixing of states. Therefore, any coherence transfer is too slow to produce an appreciable cross-polarization peak, yielding a slow anisotropy decay.

This coherence transfer mechanism has been used to explain similar dynamics in the cross-polarized 2DES of the LH2 complex of purple bacteria [27]. It indicates that the cross-polarized spectra allow the direct detection of degenerate pairs of states that can be seen as a symmetry-breaking-sensitive GB peak. Moreover, the intensity of the cross-polarized signal, markedly different between aggregates with different δ, suggests a direct link between the chirality of the system and coherence transfer processes in cylindrical molecular aggregates that can be computationally and experimentally studied using cross-polarized 2DES schemes.

In this project, cylindrical assemblies have been assumed to be the dominant secondary structures in chlorosomes [12,42]. However, mutually orthogonal transition-dipole moments do not necessarily require closed tubular molecular assemblies. Indeed, quarter-cylinder or stacked lamella-like structures are sufficient to obtain similar LD spectra shown in this work [43]. On the other hand, the cross-polarized feature in 2DES spectra requires the states with mutually orthogonal TDMs to belong in the same structure to allow non-adiabatic mixing by ultrafast coherence transfer. Therefore, the experimental measurement of this feature could be useful for acquiring further information regarding the curvature and supramolecular stacking of secondary structures in molecular aggregates.

More importantly, the cross-polarized feature shown in this project can shed light on the long-termed debate regarding the macroscopic chirality of the tubular aggregates. In particular, the experimental observation of the cross-polarized peak obtained in this work could constitute strong evidence supporting the results in reference [12] that suggest the dominance of structures with $\delta \approx 110°$. The presence of persistent features in the cross-polarized 2DES spectra of chlorosomes could be used to unambiguously assign the chirality of a cylindrical aggregate since the presence of degenerate pairs of eigenstates has been proved to be chirality dependent.

Chapter 5

Conclusions

The effect of supramolecular chirality on the optical properties of the chlorosomal LH systems is still poorly understood due to structural heterogeneity and the lack of a distinct crystalline organization that deters experimental characterization at fully atomistic resolution. Indeed, experimental results lead to contradictory results for δ. This work investigated the connection between the chirality of the chlorosomal LH complexes and their optical response using computational spectroscopic techniques within a multiscale approach based on molecular dynamics and excitonic Hamiltonians. The experimental measurement of the cross-polarized signal reported in this work could be used as strong evidence for the unambiguous determination of the chirality of the system in favor of the structure reported in reference [12]

The same computational strategy was applied to two pre-computed tubular aggregates with different chirality to identify spectral signatures of pairs of mutually orthogonal degenerate states and the dependence of such features on the chiralities. The matching of the main features in simulated and available experimental spectra shows that the theoretical model provides reliable results despite the simplifications considered in this study.

The presence (or absence) of degenerate states in the aggregates was initially determined by combining linear absorption and LD spectra. Linear spectral simulation shows that the presence of $k = \pm 1$ states signal largely accounts for the experimental FWHM of the absorption spectra. LD spectra revealed a very small magnitude of the μ_x and μ_y components for the structure with $\delta \approx 50°$, i.e., when $\beta \approx 0°$. These findings reveal that the chirality of the aggregates dictates the orientation of TDMs.

A persistent signal was found close to the diagonal region of cross-polarized 2DES of aggregate $\delta \approx 112°$. The spectral component decomposition and time-evolution of spectral

intensities helped to determine that the GB signal eventually dominates the full cross-polarized spectrum. The cross-polarized feature, therefore, arises from the ground state bleaching process. This result must be handled carefully since the closeness between the GB and EA signals, in combination with higher levels of disorder, could lead to mixed GB and EA contributions to the cross-polarized peak. Further studies will be needed to provide a more thorough interpretation of these observations.

This phenomenon was attributed to coherence transfer between the two $k \pm 1$ states during the t_1 and t_3 time periods. The molecular disorder lifts the degeneracy of the system, allowing mutually-orthogonal states to mix by coherence transfer. It was confirmed by the fast decay of the polarization anisotropy at the position of the cross-polarized peak.

The cross-polarized feature's intensity depends on the aggregate's chirality, as it is expected to appear in systems with non-neglectable perpendicular-oriented TDMs. Studies of similar dynamics on other LH systems using cross-polarized demonstrate the usefulness of polarization-controlled 2DES, supported by theoretical modeling, to study coherence dynamics in molecular aggregates. Experimentally, however, cross-polarized techniques are hard to implement. The experimental calculation of the anisotropy decay in compliment with computational spectra is an economic alternative to look for the presence of degenerate pairs. The results of this work suggest that the chirality of the chlorosome's LH system and, in general, structural features related to the orientation of TDMs and the presence of molecular disorder can be further studied computationally using cross-polarized 2DES spectroscopy schemes.

Chapter 6

Contributions

The author proposed the research question and designed the research together with prof. Dr. Thomas L.C. Jansen and Vesna Erić. All the spectral calculations were performed using the NISE software developed by T.L.C Jansen. The author created the initial structures and performed all the MD and spectroscopic calculations under the supervision of Vesna Erić. Data post-processing was performed using python scripts developed by Vesna Erić and the author. Spectroscopic simulated data, pre-computed by Vesna Erić, were used for comparison purposes. The author analyzed all the simulated spectroscopic data. The conclusions presented in the conclusion section were all drawn by the author.

Chapter 7

Acknowledgement

This Master's thesis was developed with the support of the Theoretical Chemistry and Computational Modeling (TCCM) Erasmus consortium. Part of this work was carried out on the Dutch national e-infrastructure with the support of SURF Cooperative. We thank the Center for Information Technology of the University of Groningen for their support and access to the Peregrine high-performance computing cluster.

Bibliography

[1] Benedetta Mennucci and Stefano Corni. *Nat. Rev. Chem.*, **3**(5):315–330, (2019).

[2] Gert Oostergetel, Herbert Van Amerongen and Egbert Boekema. *Photosynth. Res.*, **104**:245–55, (2010).

[3] Jakub Pšenčík, Sarah J. Butcher and Roman Tuma. *Chlorosomes: Structure, Function and Assembly*, pages 77–109. Springer Netherlands, Dordrecht, 2014.

[4] Swapna Ganapathy, Gert T. Oostergetel, Piotr K. Wawrzyniak, Michael Reus, Aline Gomez Maqueo Chew, Francesco Buda, Egbert J. Boekema, Donald A. Bryant, Alfred R. Holzwarth and Huub J. M. de Groot. *PNAS*, **106**(21):8525–8530, (2009).

[5] Xinmeng Li, Francesco Buda, Huub J.M. De Groot and G. J. Agur Sevink. *J. Phys. Chem. C*, **122**(26):14877–14888, (2018).

[6] Xinmeng Li, Francesco Buda, Huub Groot and Geert Sevink. *Science*, **25**:103618, (12 2021).

[7] Câtâlin Didraga, Joost A. Klugkist and Jasper Knoester. *J. Phys. Chem. B*, **106**(44):11474–11486, (2002).

[8] Sergei Savikhin, Paula I. van Noort, Yinwen Zhu, Su Lin, Robert E. Blankenship and Walter S. Struve. *Chemical Physics*, **194**(2):245–258, (1995). Energy Transfer and Stabilization in Plants and Bacterial Photosynthetic Reaction Centers.

[9] Jakub Dostál, Tomáš Mančal, Ramu Nas Augulis, František Vácha, Jakub Pšenčík and Donatas Zigmantas. *J. Am. Chem. Soc.*, **134**(28):11611–11617, (2012).

[10] Lisa M. Günther, Marc Jendrny, Erik A. Bloemsma, Marcus Tank, Gert T. Oostergetel, Donald A. Bryant, Jasper Knoester and Jürgen Köhler. *J. Phys. Chem. B*, **120**(24):5367–5376, (2016).

[11] Xinmeng Li. *A Computational Study of Structural and Excitonic Properties of Chlorosomes*. PhD thesis, Leiden University, 2020.

[12] Lisa M. Günther, Alexander Löhner, Carolin Reiher, Tenzin Kunsel, Thomas L. C. Jansen, Marcus Tank, Donald A. Bryant, Jasper Knoester and Jürgen Köhler. *J. Phys. Chem. B*, **122**(26):6712–6723, (2018).

[13] Felipe Cardoso Ramos, Michele Nottoli, Lorenzo Cupellini and Benedetta Mennucci. *Chem. Sci.*, **10**(42):9650–9662, (2019).

[14] Thomas L. C. Jansen and Jasper Knoester. *Acc. Chem. Res.*, **42**(9):1405–1411, (2009).

[15] Thomas L. C. Jansen, B. M. Auer, Mino Yang and J. L. Skinner. *J. Chem. Phys*, **132**(22):224503, (2010).

[16] Chungwen Liang and Thomas L. C. Jansen. *J. Chem. Theory Comput.*, **8**(5):1706–1713, (2012).

[17] Thomas L.C. Jansen. *J. Chem. Phys.*, **155**(17), (2021).

[18] M. D. Galanin: V. M. Agranovich. *Ber. Bunsenges. Physik. Chem.*, **88**(7):687–687, (1984).

[19] Anna Bondarenko. *Modeling of excitonic properties in tubular molecular aggregates*. PhD thesis, University of Groningen, 2019.

[20] Tenzin Kunsel, Alexander Lôhner, Jack Mayo, J Kôhler, Thomas L.C Jansen and J Knoester. *J. Chem. Phys*, **153**:134304, (2020).

[21] Anna S. Bondarenko, Ilias Patmanidis, Riccardo Alessandri, Paulo C. T. Souza, Thomas L. C. Jansen, Alex H. de Vries, Siewert J. Marrink and Jasper Knoester. *Chem. Sci.*, **11**:11514–11524, (2020).

[22] Shu Furumaki, Frantisek Vacha, Satoshi Habuchi, Yusuke Tsukatani, Donald A. Bryant and Martin Vacha. *J. Am. Chem. Soc.*, **133**(17):6703–6710, (2011).

[23] Thomas L.C. Jansen and Jasper Knoester. *J. Phys. Chem. B*, **110**(45):22910–22916, (2006).

[24] Peter Hamm and Martin Zanni. *Concepts and Methods of 2D Infrared Spectroscopy*. Cambridge University Press, 2011.

[25] S. Mukamel. *Principles of Nonlinear Optical Spectroscopy*. Oxford University Press, 1995.

[26] Gregory S. Engel, Tessa R. Calhoun, Elizabeth L. Read, Tae Kyu Ahn, Tomáš Mančal, Yuan Chung Cheng, Robert E. Blankenship and Graham R. Fleming. *Nature*, **446**(7137):782–786, (2007).

[27] Andy S. Sardjan, Floris P. Westerman, Jennifer P. Ogilvie and Thomas L.C. Jansen. *J. Phys. Chem. B*, **124**(42):9420–9427, (2020).

[28] Tessa R. Calhoun Tomáš Mančal Tae Kyu Ahn Robert E. Blankenship Graham R. Fleming Elizabeth L. Read, Gregory S. Engel. *PNAS*, **104**(36):14203–14208, (2007).

[29] Xinmeng Li. Ctubegen, (2020). https://github.com/xinmeng2015/chlorosome_phd_thesis.

[30] Mark James Abraham, Teemu Murtola, Roland Schulz, Szilárd Páll, Jeremy C. Smith, Berk Hess and Erik Lindahl. *SoftwareX*, **1-2**:19–25, (2015).

[31] William L. Jorgensen, David S. Maxwell and Julian Tirado-Rives. *Journal of the American Chemical Society*, **118**(45):11225–11236, (1996).

[32] George A. Kaminski, Richard A. Friesner, Julian Tirado-Rives and William L. Jorgensen. *J. Phys. Chem. B*, **105**(28):6474–6487, (2001).

[33] Giovanni Bussi, Davide Donadio and Michele Parrinello. *J. Chem. Phys*, **126**(1):014101, (2007).

[34] M. Belén Oviedo and Cristián G. Sánchez. *J. Phys. Chem. A*, **115**(44):12280–12285, (2011).

[35] Valentin I Prokhorenko and R.J. van Grondelle, Rienk Dwayne Miller. *Photon Echo Study of the Electron-Phonon Coupling Strength in Molecules and Molecular Aggregates. Ultrafast Phenomena XIV*, pages 601–603, Berlin, Heidelberg, 2005. Springer Berlin Heidelberg.

[36] Dominik Lindorfer and Thomas Renger. *J. Phys. Chem. B*, **122**(10):2747–2756, (2018).

[37] Gabriela S Schlau-Cohen, Akihito Ishizaki, Tessa R Calhoun, Naomi S Ginsberg, Matteo Ballottari, Roberto Bassi and Graham R Fleming. *Nat. Chem*, **4**(5):389–395, (2012).

[38] Tobias Kramer and Mirta Rodríguez. *Photosynth. Res.*, **144**(2):147–154, (2020).

[39] Erling Thyrhaug, Roel Tempelaar, Marcelo J P Alcocer, Karel Žídek, David Bína, Jasper Knoester, Thomas L C Jansen and Donatas Zigmantas. *Nature chem*, **10**(7):780–786, (2018).

[40] Sebastian Westenhoff, David Palecěk, Petra Edlund, Philip Smith and Donatas Zigmantas. *J. Am. Chem. Soc.*, **134**(40):16484–16487, (2012).

[41] Robin M. Hochstrasser. *Chem. Phys.*, **266**(2-3):273–284, (2001).

[42] Xinmeng Li, Francesco Buda, Huub J. M. de Groot and G. J. Agur. Sevink. *J. Phys. Chem. C*, **123**(26):16462–16478, (2019).

[43] Lisa M. Günther, Jasper Knoester and Jürgen Köhler. *Molecules*, **26**(4), (2021).